catalysts

MDPI

Article

In Situ Preparation of 0D/2D Zn-Ag-In-S Quantum Dots/RGO Heterojunctions for Efficient Photocatalytic Hydrogen Production

Bangya Deng [1], Yalin Yang [1], Afaq Ullah Khan [1], Qitao Chen [1], Xianjin Wang [1], Tong Ren [1], Jiaji Li [1], Yanhong Liu [1,*], Lixia Li [2,*] and Baodong Mao [1,*]

[1] School of Chemistry and Chemical Engineering, Jiangsu University, Zhenjiang 212013, China; 2212112047@stmail.ujs.edu.cn (B.D.); 201810005@fzu.edu.cn (Y.Y.); afaqchemist@gmail.com (A.U.K.); 2112212007@stmail.ujs.edu.cn (Q.C.); 2222112031@stmail.ujs.edu.cn (X.W.); 2212212051@stmail.ujs.edu.cn (T.R.); 2222212030@stmail.ujs.edu.cn (J.L.)

[2] School of the Environment and Safety Engineering, Jiangsu University, Zhenjiang 212013, China

* Correspondence: liuyh@ujs.edu.cn (Y.L.); qingpipa@ujs.edu.cn (L.L.); maobd@ujs.edu.cn (B.M.)

Abstract: The creation of junctions between 0D and 2D materials can be an efficient strategy to enhance charge separation for solar hydrogen production. In this study, a simple in situ growth method has been used to synthesize a series of 0D/2D Zn-Ag-In-S quantum dots/reduced graphene oxide (ZAIS QDs/RGO) heterojunctions. The developed heterojunctions were characterized for structural characteristics, morphology, and photocatalytic performance, while varying the content of RGO. We observed that photocatalytic hydrogen production reached a maximum at an RGO content of 30 µL (342.34 µmol g^{-1} h^{-1}), surpassing that of pure ZAIS QDs (110.38 µmol g^{-1} h^{-1}) by 3.1 times, while maintaining excellent stability. To understand this enhancement, we performed time-resolved fluorescence and electrochemical impedance spectroscopy. The fluorescence lifetime of RGO loaded at 30 µL (417.76 ns) was significantly higher than that of pure ZAIS QDs (294.10 ns) and had the fastest charge transfer, which can be attributed to the charge transfer and storage capacity of RGO to extend the lifetime of photogenerated carriers and improve the charge separation efficiency. This study offers a simple synthesis method for constructing 0D/2D QDs/RGO heterojunction structures and provides a valuable reference for further enhancing the activity and stability of I-III-VI sulfide QDs.

Keywords: photocatalysis; quantum dots; reduced graphene oxide; 0D/2D heterostructure; hydrogen production

Citation: Deng, B.; Yang, Y.; Khan, A.U.; Chen, Q.; Wang, X.; Ren, T.; Li, J.; Liu, Y.; Li, L.; Mao, B. In Situ Preparation of 0D/2D Zn-Ag-In-S Quantum Dots/RGO Heterojunctions for Efficient Photocatalytic Hydrogen Production. *Catalysts* **2023**, *13*, 1471. https://doi.org/10.3390/catal13121471

Academic Editor: Roberto Fiorenza

Received: 28 October 2023
Revised: 16 November 2023
Accepted: 21 November 2023
Published: 27 November 2023

1. Introduction

Harnessing solar energy for photocatalytic hydrogen production is seen as the ultimate solution to energy shortage as the world faces a growing demand for energy [1,2]. One of the crucial factors in the process of photocatalytic hydrogen production is finding suitable photocatalysts [3,4]. In this context, there is an increasing focus on designing photocatalysts with low cost, high activity, and high stability for efficient hydrogen production [5–7]. Extensive research into the synthesis, properties, and applications of III-V and II-VI semiconductors has been carried out over the last few decades [8]. However, traditional II-VI semiconductor quantum dots (QDs) often contain toxic elements such as Hg, Cd, and Pb, which have adverse effects on the environment and health. This has resulted in significant limitations in the use of III-V and II-VI semiconductors [9]. Consequently, the exploration of nanomaterials with low toxic elements is of paramount importance for societal progress. The I-III-VI QD has attracted considerable interest among researchers because of its exceptional optical properties and ability to efficiently absorb solar energy [10]. Specifically, ZAIS QDs have emerged as key players in visible light catalysis within the realm of photocatalysis [11]. These QDs offer several advantages, including the use of

non-toxic constituents, straightforward synthesis methods, remarkable optical properties, tunable emission wavelengths, and a superior quantum size effect [12].

There are some drawbacks associated with the use of ZAIS QDs in photocatalysis that need to be considered. The efficiency of photocatalytic hydrogen production is reduced by the rapid recombination of photogenerated carriers in ZAIS QDs and the tendency of photocatalysts to agglomerate [13,14]. This issue can be addressed by introducing 2D nanosheets to form 0D/2D heterojunction structures. To this end, reduced graphene oxide (RGO)—a non-metallic 2D carbon material—is a promising candidate that offers a large surface area for adsorption, exhibits high chemical stability and transmittance, and has significant electron-accepting and donating properties [15–17]. Therefore, integrating RGO into a photocatalytic system can significantly enhance charge separation efficiency and serve as an electron storage device [18,19]. In a study by Chen et al. a $ZnIn_2S_4$/RGO composite photocatalyst was synthesized using a one-pot hydrothermal method and showed excellent performance and stability in the photocatalytic degradation of 4-nitrophenol [20]. Similarly, Lv et al. synthesized a $LaNiO_3$-RGO composite structure through a simple self-assembled photocatalytic reduction method, demonstrating exceptional photocatalytic activity [21]. Kudo et al. constructed a system combining RGO and $CuGaS_2$ in a Z-shaped configuration. RGO served as an electronic medium by adsorbing photogenerated charges on its surface, facilitating effective electron transfer, and enhancing the photocatalytic decomposition of water [22]. I-III-VI nanocrystals and RGO composites have also been explored. For instance, Xie et al. utilized a one-step solvothermal method to anchor nano-$CuInS_2$ onto RGO nanosheets. The results revealed significantly higher photocatalytic activity for RGO/$CuInS_2$ compared to pure $CuInS_2$. Despite the fact that the photocatalytic activity of RGO/$CuInS_2$ is twice as high as that of pure $CuInS_2$, detailed mechanistic studies are still lacking [23].

In this study, we successfully synthesized ZAIS/RGO heterojunctions by combining 0D and 2D materials using an in situ hydrothermal method. The photocatalytic hydrogen production performance of ZAIS QDs was significantly enhanced by the addition of RGO. Notably, when we used 30 µL of RGO, the photocatalytic hydrogen production rate reached an impressive 342.34 µmol g^{-1} h^{-1}. This was a 3.10-fold increase compared to pure ZAIS, and this compound also demonstrated exceptional photocatalytic stability. The improved photocatalytic activity in the 0D/2D heterojunction system can be primarily attributed to effective carrier separation. The time-resolved fluorescence analysis revealed a significantly extended surface carrier lifetime, reaching 417.76 ns, compared to pure ZAIS QDs (294.10 ns). This was possible because RGO acted as an electronic reservoir, capturing ZAIS excited-state electrons and reducing the electron–hole pair recombination rate. Additionally, the large surface area of RGO provided an abundance of active sites for photocatalytic hydrogen production in the composite photocatalytic converters. The in situ assembly method for synthesizing ZAIS and RGO played a crucial role in the results achieved. It created strong bonds at the QD surface, enhancing the proximity and stability of the connection between ZAIS and RGO. This study offers valuable insights and lays the groundwork for designing and synthesizing highly efficient photocatalysts.

2. Results and Discussion

In Figure 1a, the XRD patterns show three distinct peaks at 27.5°, 46.4°, and 54.4°, indicating (102), (110), and (022) cubic phase planes of ZAIS (JCPDS No. 25–1329), respectively [24]. It can be seen that there is no significant shifting in the diffraction peaks, indicating that the incorporation of RGO did not alter the structure in addition to the composition of the samples. In Figure 1a, we can also see that the intensity of the diffraction peak is lower than that of pure QDs, which may be due to the uniform distribution of ZAIS QDs on RGO nanosheets after the introduction of RGO, which reduces the aggregation of QDs and leads to the weakening of the intensity of the diffraction peak of XRD [25]. Moreover, the composition of the ZAIS QDs, prepared according to the specified procedure, was examined using energy dispersive X-ray (EDX) analysis. The EDX analysis of the

QD, as depicted in Figure 1b, revealed the presence of Ag, In, Zn, C, and S elements. This outcome signifies the successful incorporation of these elements, corroborating the effective in situ incorporation of RGO within the heterojunction structure. The presence of these elements, as evidenced by the EDX results, further supports the integrity of the composite structure, and underscores the successful synthesis of the ZAIS/RGO composite material with the desired elemental composition.

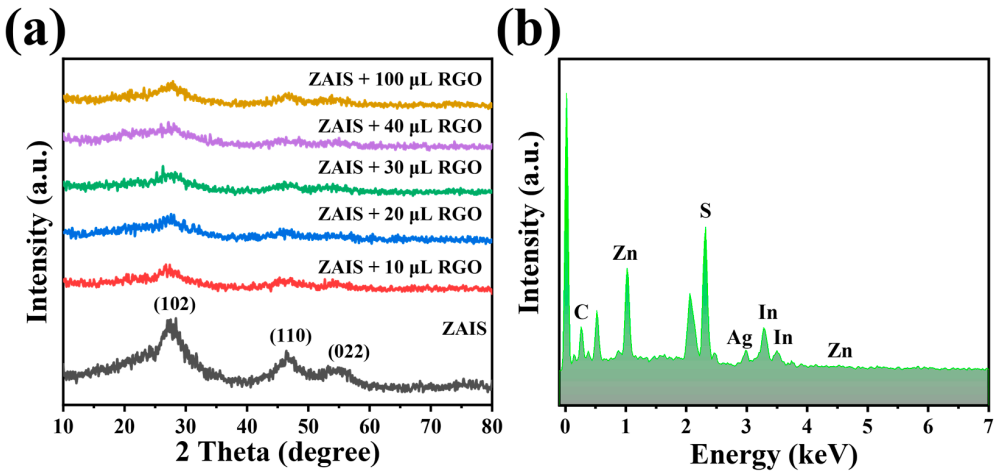

Figure 1. (**a**) XRD patterns of ZAIS QDs with varying amounts of RGO; (**b**) EDX spectrum of ZAIS QDs with 30 µL of RGO.

As shown in Figure 2a, the TEM analysis of ZAIS QDs reveals a particle size of approximately 6.51 ± 1.0 nm. In Figure 2b, we can see that RGO nanosheets are almost transparent under TEM, indicating that RGO nanosheets have a very thin nanostructure. And in Figure 2c, we can see that ZAIS QDs are uniformly distributed on RGO nanosheets. It is evident from Figure 2d that the dimensions of ZAIS QDs are several nanometers. The lattice fringes at 0.38 nm correspond to (220) crystal planes, and the particle distribution is more uniform. This indicates that the QDs are successfully loaded on RGO nanosheets by the in situ hydrothermal method, and the synthesis, microstructure, and lattice structure of the pure QDs are not affected by the incorporation of ZAIS QDs into RGO nanosheets.

FT-IR was carried out to explore the types of chemical bonds within ZAIS/RGO QDs and to detect ZAIS QDs anchored on graphene nanosheets through functional groups. An in situ growth method was used. As shown in Figure 3a,b, the infrared absorption band at 3648–3299 cm^{-1} has been identified as the tensile vibration mode of the hydrogen bonds in the compounds [26,27]. The absorption peaks at 1610.2, 1388.5, and 1088 (1015.5) cm^{-1} are assigned to the tensile vibration modes of C=O, O–H, and C–O, respectively [28–30]. From the enlarged figure of Figure 3b, we can see that the two characteristic peaks of C=O and C–O have obvious enhancement compared with that of ZAIS QDs from the addition of RGO, and the peak is strong when the RGO content is 20 µL. This indicates that bonding between ZAIS QDs and RGO surface occurs; thus, the functional groups of C=O and C—O increase gradually. Bonding gives the composite photocatalyst good stability and good hydrophilic and dispersive properties. However, with increasing RGO, the intensity of the two peaks decreases gradually. A possible reason is that excessive RGO is wrapped on the surface of QDs, which reduces the contact area between the two photocatalysts and hinders the bonding reaction. The broadband region of 3400–3800 cm^{-1} and 2368 cm^{-1} may be due to the physical adsorption of H_2O and CO_2 in air [31,32]. This indicates that the surface of RGO and ZAIS QDs have a strong interaction, which makes the combination of RGO and ZAIS QDs more closely spaced, thus reducing the distance of charge transfer, improving the rate of charge transfer between them, and enhancing the photocatalytic performance.

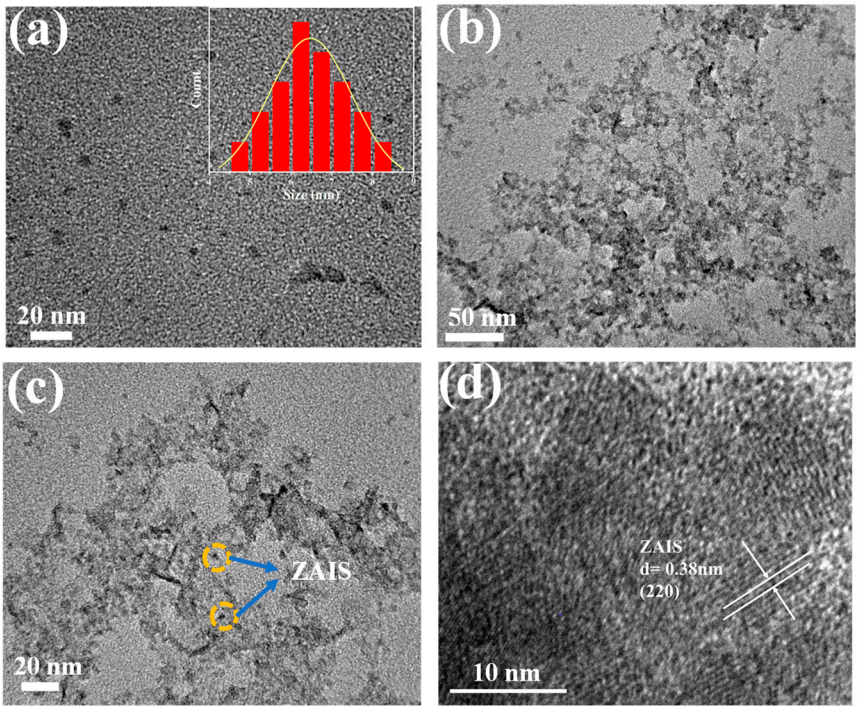

Figure 2. (**a**) TEM images of ZAIS QDs (inset in (**a**) size distribution histogram). ZAIS/RGO-30 μL composites: (**b**,**c**) TEM and (**d**) HRTEM.

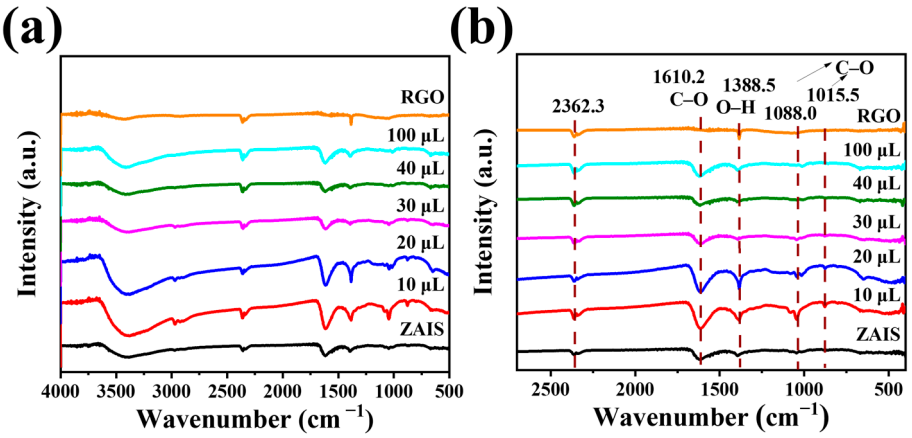

Figure 3. (**a**) FT-IR spectra of ZAIS/RGO with various samples. (**b**) FT-IR spectra of ZAIS/RGO with the local magnification of (**a**).

XPS measurements were carried out for further analysis of the electronic state and chemical composition of the prepared photocatalysts. From Figure 4a, the XPS survey spectra contain Zn, In, Ag, C, and S elements, and the results indicate the ZAIS QDs were successfully deposited on the surface of RGO. In Figure 4b, two peaks at 368.0 and 374.1 eV are observed for ZAIS QDs and ZAIS QDs-30 μL RGO, which can be attributed to the binding energies of Ag $3d_{5/2}$ and $3d_{3/2}$, and neither show any blue shifts [33]. In Figure 4c, the peaks at 452.7 and 445.2 eV (30 μL) and the peaks at 452.5 and 445.0 eV (ZAIS QDs) are attributed to In $3d_{3/2}$ and In $3d_{5/2}$, respectively, indicating the presence of In^{3+} species in the sample [34,35]. In Figure 4d, the peaks at 1022.2 and 1045.3 eV in pure ZAIS QDs correspond to Zn $2p_{1/2}$ and Zn $2p_{3/2}$, while the peaks in ZAIS QDs-30 μL RGO are shifted to 1022.4 and 1045.5 eV, respectively, compared to pure QDs [36,37]. A significant shift in ZAIS QDs-30 μL corresponding to In 3d and Zn 2p was observed, whereas a slight shift corresponding to S-elements was also observed in comparison with pure QDs. The two peaks appearing at 161.6 and 162.8 eV in Figure 4e could be attributed to both pure QDs and ZAIS

QDs-30 μL RGO, as both of them correspond to S $2p_{3/2}$ and S $2p_{1/2}$. These two peaks show a slight blue shift of 0.2 eV in the case of ZAIS QDs-30 μL RGO, appearing at 161.8 and 163.0 eV, respectively [38,39]. The change in the XPS peak is mainly due to the decrease in the electron cloud density on the surface of the composite photocatalysts, indicating that charge transfer occurs between the ZAIS QDs and the RGO interface in the composite photocatalysts. The surface electron concentration of RGO decreases and that of ZAIS QDs increases, which indicates that RGO can be used as a charge storage device in composite photocatalysts. As shown in Figure 4f, composite photocatalysts can be fitted into three peaks, which are located at 288.7 eV, 286.0 eV, and 284.7 eV, respectively, corresponding to the extensional oscillation of C=O, C–O, and C–C functional groups [40,41]. The results of infrared measurements can also further prove that ZAIS QDs and RGO have a strong interaction, which also promotes photogenerated charge transfer and photocatalytic hydrogen production.

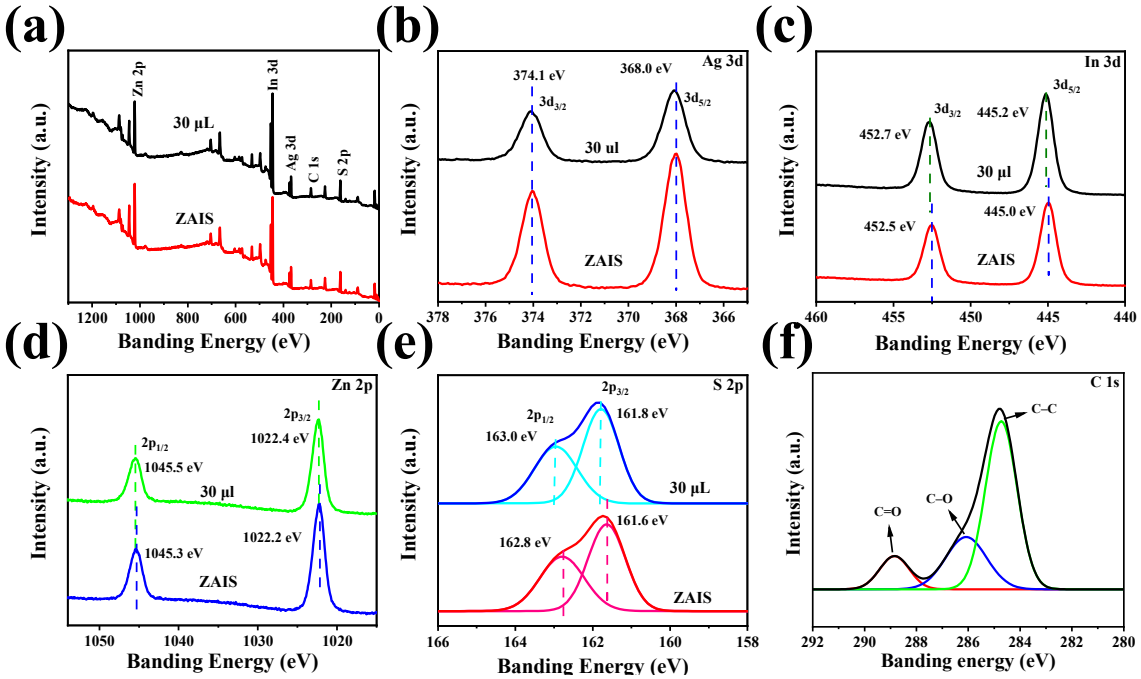

Figure 4. XPS spectra of ZAIS QDs and ZAIS QDs modified with 30 μL RGO: (**a**) survey, and high-resolution spectra of (**b**) Ag 3d, (**c**) In 3d, (**d**) Zn 2p, (**e**) S 2p and (**f**) C 1s.

To evaluate the photocatalytic performance of the QDs with Na_2S (0.35 M) and Na_2SO_3 (0.25 M) as sacrificial reagents, photocatalytic hydrogen production was performed. Photocatalytic hydrogen production experiments using composite photocatalysts loaded with different amounts of RGO were carried out. As shown in Figure 5a, the photocatalytic H_2 production of ZAIS QDs composite photocatalysts increased linearly with the illumination time. For the pure QDs, the hydrogen content reached 110.38 μmol g^{-1} h^{-1} within 6.5 h under visible light exposure (Figure 5a, Table 1). It is quite evident from Figure 5b that H_2 evolution (342.34 μmol g^{-1} h^{-1}) of ZAIS/RGO composite is 3.1 times higher than that of pure QDs, indicating that RGO can be used as a co-catalyst to enhance hydrogen gas evolution. Under visible light, the photocatalyst was stimulated to generate electrons and holes, and the electrons were transferred to the RGO surface for photocatalytic hydrogen production, which will reduce the recombination of electrons/holes and increase the recombination rate of electron holes. However, when the amount of RGO was above 30 μL, photocatalytic H_2 production showed a downward trend, which may be due to excessive RGO concealing the active sites on the surface of ZAIS QDs, which reduces the active sites for photocatalytic hydrogen production. On the other hand, loading excessive RGO weakened the interaction between RGO and ZAIS QDs. Our results also show that electron–hole

separation efficiency is an important factor affecting photocatalytic activity. Therefore, it is very important to choose a suitable loading level in the photocatalytic system.

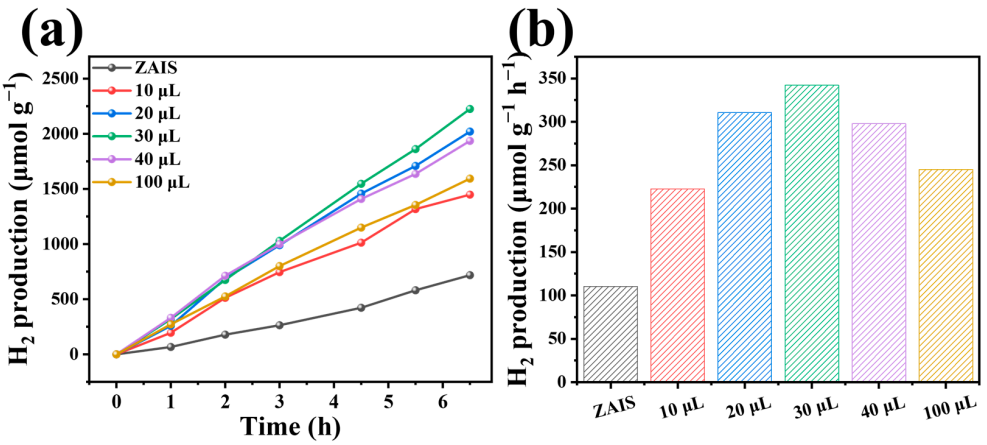

Figure 5. (**a**) Time curves of photocatalytic hydrogen production and (**b**) hydrogen production rate of ZAIS QDs with different amounts of RGO.

Table 1. Comparison of hydrogen production of the related photocatalysts.

Catalysts	Light Source	Reaction Conditions	H_2 Evolution Rate ($\mu mol\ g^{-1}\ h^{-1}$)	Ref.
ZAIS/RGO	$\lambda \geq 400$ nm	0.35 M Na_2S + 0.25 M Na_2SO_3	342.34	This work
CdS-rGO/HI	$\lambda \geq 400$ nm	0.35 M Na_2S + 0.25 M Na_2SO_3	76.6	[42]
$Cs_2AgBiBr_6$/RGO	$\lambda \geq 400$ nm	saturated HBr and H_3PO_2 solution	48.9	[33]
h-BN/rGO		15 vol% TEOA	157.63	[43]
MoS_2/RGO	$\lambda \geq 400$ nm	0.1 M Na_2S + 0.6 M Na_2SO_3	4.86	[40]
Ru(dcbpy)$_3$/TiO_2/RGO/Pt	$\lambda \geq 400$ nm	EDTA	191.8	[44]
$BiPO_4$/RGO		5 vol% ethanol	306	[45]
TiO_2-rGO	$\lambda \geq 400$ nm	25 vol% methanol	35	[46]

For the practical application of photocatalysis, the stability of the photocatalyst is of great importance. Therefore, the stability of ZAIS QDs and 30 μL RGO photocatalyst was tested. As shown in Figure 6a, the photocatalytic activity of the ZAIS QDs decreased by 12.72% after three reaction cycles when exposed to visible light irradiation ($\lambda > 420$ nm). In Figure 6b, we can see that the photocatalytic hydrogen production rate of ZAIS-30 μL RGO QDs was reduced by a 4% ratio after three runs of photocatalytic hydrogen production reaction. In conclusion, the composite photocatalyst has high photocatalytic stability, which can be attributed to the interaction between ZAIS QDs and RGO, and which makes the photocatalyst have high stability in photocatalytic hydrogen production experiments.

To elucidate the intricate mechanisms underpinning the variations in photocatalytic activity of the composite photocatalysts, an in-depth analysis was undertaken employing UV-vis absorption spectra, Tauc plots, and XPS valence band methodologies. The UV-vis absorption spectra, as illustrated in Figure 7a, reveal notable visible light absorption characteristics for ZAIS QDs with varying amounts of RGO. The Tauc plots (Figure 7b) and XPS valence band plots provided clear insights, indicating an energy bandgap (Eg) of 1.93 eV and a valence band (VB) of 0.96 eV for ZAIS, respectively. Utilizing the formula Eg = VB − CB, we determined the conduction band (CB) of ZAIS to be −0.97 eV. Furthermore, Figure 7c presents the corresponding bandgap of ZAIS alongside our hypothesized response mechanism. To elucidate the proposed reaction mechanism of the ZAIS/RGO composite photocatalysts, we explored time-resolved photoluminescence (TRPL) spectra under 485 nm laser excitation and employed electrochemical impedance spectroscopy (EIS) to validate our conjectures. In Figure 7d, ZAIS/RGO photocatalysts exhibit obvious

photoluminescence (PL) quenching in contrast to ZAIS QDs at the emission peak of 635 nm. The fluorescence lifetime can reflect photogenerated charge carrier recombination and transfer. As shown in Figure 7e, A biexponential function was fitted to the TRPL decay curves of the QDs by $I(t) = A_1 * \exp\left(\frac{-t}{\tau_1}\right) + A_2 * \exp\left(\frac{-t}{\tau_2}\right)$ and the average lifetime is estimated by $\tau_{ave} = \left(A_1{\tau_1}^2 + A_2{\tau_2}^2\right)/\left(A_1\tau_1 + A_2\tau_2\right)$. The delay strength is represented by $I(t)$ in TRPL. τ_1 and τ_2 express the composite lifetimes and can be represented by A_1 and A_2, giving the relative weight of the decay components at $t = 0$. A shorter fluorescence lifetime due to the surface defects of semiconductors, and intrinsic defects, will lead to a longer fluorescence lifetime of semiconductors. As shown in Table 2 the fluorescence lifetime of 30 µL RGO-loaded ZAIS QDs is significantly longer than that of pure ZAIS QD, 417.76 ns versus 294.10 ns, respectively, and that of 100 µL RGO-loaded ZAIS QDs (330.78 ns) is higher than that of pure ZAIS QDs (294.10 ns). This observation indicates that introducing RGO into ZAIS QDs can reduce the surface defects of QDs. At the same time, metal ions in ZAIS QDs transfer to the surface of RGO, which will increase the internal defects of QDs and increase fluorescence lifetime. However, excessive RGO will cover up the reactive sites of ZAIS QDs and affect the internal metal ions of ZAIS QDs transfer to the RGO surface, leading to a decrease in the lifetime of the sample. Therefore, it is necessary to introduce a suitable amount of RGO to improve photocatalytic performance. In order to further investigate the electron-hole transport efficiency and the separation efficiency of photocatalysts, electrochemical impedance measurements were performed. EIS is also an effective technique for studying the charge separation process at the semiconducting electrolytic interface. The arc is smaller and the resistance of the photocatalyst carriers is weaker in the transport process, which will better show the electron-hole separation efficiency. As shown in Figure 7f, the impedance of the ZAIS-30 µL RGO QDs with the highest hydrogen precipitation rate is smaller than that of the other two samples. This indicates that the RGO photocatalyst with a loading of 30 µL has the fastest charge transfer, and this result demonstrates that the composite catalyst has the highest electron–hole separation efficiency.

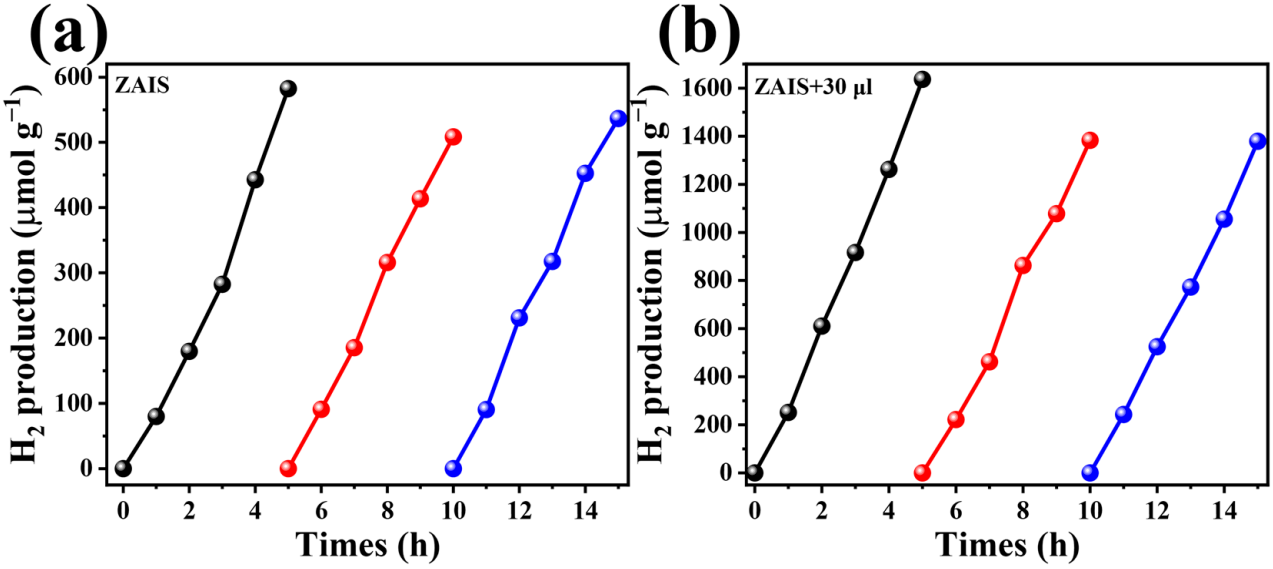

Figure 6. (**a**) Study of photocatalytic stability of ZAIS QDs; (**b**) photocatalytic stability of ZAIS QDs capped 30 µL RGO.

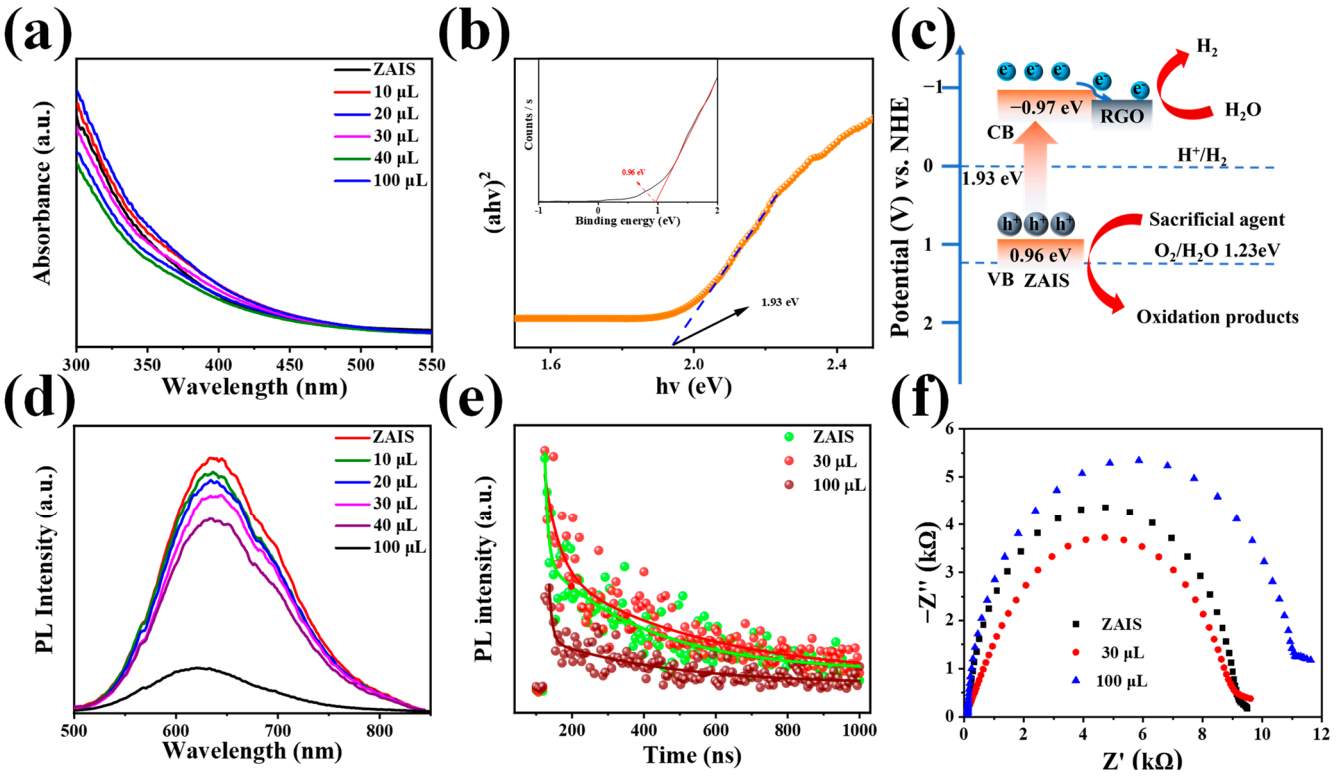

Figure 7. (**a**) UV-vis absorption spectra of ZAIS QDs with different amounts of RGO. (**b**) Tauc plots of ZAIS QDs (inset in (**b**): XPS valence band spectra). (**c**) Corresponding band alignment of ZAIS and RGO. (**d**) PL spectra of ZAIS QDs with different amounts of RGO. (**e**) TRPL decay curves and (**f**) EIS of ZAIS QDs and ZAIS QDs loaded with 30 or 100 μL RGO.

Table 2. TRPL decay data for ZAIS QDs and ZAIS QDs loaded with 30 and 100 μL RGO.

Samples	A_1/%	τ_1/ns	A_2/%	τ_2/ns	τ_{ave}/ns
ZAIS	2.90	8.93	97.10	294.36	294.10
30 μL	10.17	39.78	89.83	421.79	417.76
100 μL	2.67	9.01	97.33	331.02	330.78

Drawing upon the aforementioned results and discussion, a plausible mechanism for photocatalytic hydrogen production by the ZAIS/RGO composite photocatalyst is proposed. As illustrated in Figure 8, the ZAIS QDs are effectively stimulated under visible light, initiating the generation of electron–hole pairs. Subsequently, the electrons generated by the light absorption jump from the valence band to the conduction band. The photogenerated electrons are then efficiently transferred from the semiconductor to the surface of RGO through the interface formed by ZAIS QDs and RGO. This orchestrated process facilitates the reaction of these electrons with water, leading to the photocatalytic production of hydrogen. Concurrently, RGO exhibits the capacity to store and transport electrons originating from ZAIS QDs. This dual role of RGO contributes to the effective separation of photogenerated electrons and holes. Following the migration of electrons, the photogenerated holes are sacrificed by reacting with the hole sacrificial agent situated on the valence band. This intricate interplay of processes enhances the photocatalytic activity of the ZAIS/RGO composite photocatalyst. In essence, the proposed mechanism underscores the synergy between ZAIS QDs and RGO, elucidating their complementary roles in promoting efficient charge transfer and utilization, ultimately leading to improved photocatalytic performance for hydrogen production.

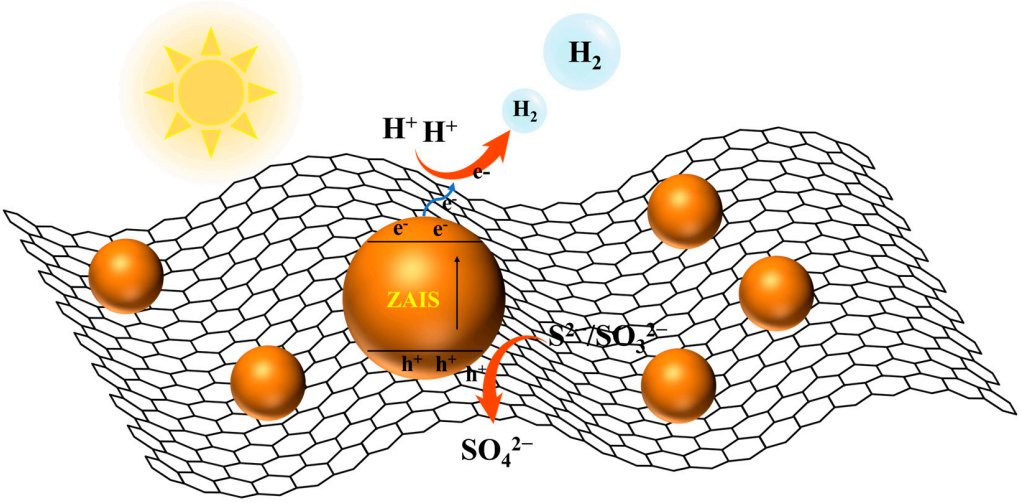

Figure 8. Photocatalytic mechanism of ZAIS/RGO composite photocatalysis for hydrogen production.

3. Experimental

3.1. Materials

Thiourea, zinc acetate ($Zn(OAc)_2 \cdot 2H_2O$), sodium hydroxide (NaOH), Mercaptopropionic acid (MPA), L-cysteine (Cys, $HSCH_2CH(NH_2)CO_2H$), indium nitrate ($In(NO_3)_3 \cdot 4.5H_2O$), sodium sulfide (Na_2S), silver nitrate ($AgNO_3$), sodium sulfite (Na_2SO_3), and thioacetamide (TAA) were purchased from Sinopharm Chemical Reagent Co., Ltd. (Guangzhou, China) and were of analytical grade.

3.2. Preparation of Photocatalysts

The previously reported method was used to prepare the RGO nanosheets [47]. ZAIS/RGO QDs with a ratio of MPA/Cys = 4:6 was prepared by an in situ hydrothermal method with the following modifications [48]. After adjusting the pH, varying quantities of RGO (1 mmol/mL) were introduced and sonicated for 30 min. Subsequently, they were moved to a 50 mL Teflon-lined stainless-steel autoclave (Xi'an Hongchen Instrument Equipment Co., Ltd., Xi'an, China), sealed, and maintained at 110 °C for 4 h. After gradual cooling to room temperature in an autoclave, the initial solution was washed three times with water/ethanol and dispersed in an aqueous solution for further experimentation and characterization.

3.3. Characterizations

The prepared samples were subjected to phase composition analysis by X-ray diffraction (XRD, D8 ADVANCE, Bruker, Rheinstetten, Germany) using a Cu-Kα radiation source (λ = 1.54056 Å) at a scan rate of 4.0° min^{-1}. The sample was analyzed by transmission electron microscopy (TEM) using a Tecnai G2 F30 S-Twin (FEI Company, Hillsboro, OR, USA) at 200 kV accelerating voltage. Functionalities were determined using the standard KBr disc method on a Nicolet NEXUS 470 (Thermo Nicolet Corporation, Madison, WI, USA) for FTIR analysis. The surface and chemical composition of the samples were determined by XPS using a Thermo ESCALAB 250 X spectrometer (Waltham, MA, USA) equipped with a 150 W Al source. The UV-vis spectrophotometric analysis was performed using a Cary 8454 spectrophotometer (Agilent Technologies Inc., Shanghai, China); however, the PL of the sample was analyzed at an excitation wavelength of 485 nm using a Cary Eclipse fluorescence spectrophotometer (Agilent Technologies Inc., Shanghai, China). EIS was performed at room temperature using a 760B electrochemical workstation (CH Instruments, Inc., Shanghai, China), with the samples uniformly distributed on FTO glass and a platinum–carbon electrode.

3.4. Photocatalytic Performance Evaluation

A multi-channel photochemical reaction device (white LED monochromatic light source, λ > 420 nm, PCX-50B Discover, Beijing Perfect Light Co., Ltd., Beijing, China) was used to evaluate photocatalytic hydrogen production. Typically, sacrificial reagents of 0.35 M Na_2S and 0.25 M Na_2SO_3 were dispersed in 20 mg of photocatalysts in a 20 mL solution. The glass bottle containing the solution mixture was placed in an ultrasonic bath until the complete dissolution of the sacrificial agent. Next, the samples were sealed, and N_2 gas was introduced to this solution for 15 min before placement inside the photoreactor (white LED monochromatic light source, λ > 420 nm, PCX-50B Discover, Beijing Perfect Light Co., Ltd., Beijing, China). The hydrogen production rate was analyzed using a gas chromatograph GC-7900 (Education Au-light Co., Ltd., Beijing, China), TCD detector (Nuoyi Instrument Co., Ltd., Shanghai, China). To determine the rate of hydrogen production, 1 mL of the gas produced is withdrawn and injected into the gas chromatograph every hour.

4. Conclusions

In summary, we synthesized a series of ZAIS/RGO composite photocatalysts loaded with varying amounts of RGO through a simple in situ growth method. Then, the photocatalytic hydrogen production performance and its potential mechanism were extensively studied. Through a hydrothermal reaction, ZAIS QDs and RGO were tightly bonded, enhancing the fluorescence lifetime, photocatalytic activity, and stability of the ZAIS/RGO composite photocatalyst. The optimum amount of RGO was adjusted in order to study the structural, optical, and photocatalytic properties of the composite photocatalyst. The study showed that the composite photocatalyst achieved a maximum photocatalytic hydrogen production rate of 342.34 μmol g^{-1} h^{-1} when the RGO content was 30 μL. This value was 3.1 times higher than that of pure ZAIS QDs, demonstrating excellent stability. Additionally, the composite exhibited a fluorescence lifetime of 417.76 ns, longer than that of pure QDs. In comparison, after three cycles of photocatalytic hydrogen production experiments, the hydrogen production rate of pure ZAIS QDs decreased by 12.72%, whereas ZAIS-30 μL RGO QDs only decreased by 4%. The mechanism of photocatalytic hydrogen production by the ZAIS/RGO composite photocatalyst was also proposed by studying the fluorescence lifetime and electrochemical impedance measurements. The study found that RGO served as an electric medium, storing electrons from ZAIS QDs, and facilitating their transportation. By efficiently separating the photogenerated electrons and holes, this process significantly improved the photocatalytic performance. The results of this investigation offer important perspectives for the improvement of the efficiency of the splitting of photogenerated electron–hole pairs and for the construction of efficient composite photocatalysts.

Author Contributions: Data curation, B.D.; Writing–original draft, B.D.; Writing–review & editing, B.D., Y.Y., Q.C., A.U.K. and B.M.; Investigation, B.D. and Y.Y.; Validation, X.W. and J.L.; Visualization, T.R.; Supervision, Y.L. and L.L.; Resources, B.M.; Funding acquisition, A.U.K., Y.L. and B.M. All authors have read and agreed to the published version of the manuscript.

Funding: This work was supported by the National Natural Science Foundation of China (22278194 and 21908081) and the Jiangsu Provincial Excellent Postdoctoral Program (2023ZB856).

Data Availability Statement: Data are contained within the article.

Conflicts of Interest: The authors declare no conflict of interest.

References

1. Onneken, C.; Morack, T.; Soika, J.; Sokolova, O.; Niemeyer, N.; Mück-Lichtenfeld, C.; Daniliuc, C.G.; Neugebauer, J.; Gilmour, R. Light-enabled deracemization of cyclopropanes by Al-salen photocatalysis. *Nature* **2023**, *621*, 753–759. [CrossRef] [PubMed]
2. Yigao, Y.; Linan, Z.; Hossein, R.; Junwei, L.B.; Jingyi, Z.; Aaron, B.; Lin, Y.; Minghe, L.; Minhan, L.; Suman, K.; et al. Earth-abundant photocatalyst for H_2 generation from NH_3 with light-emitting diode illumination. *Science* **2022**, *378*, 889–893. [CrossRef]

3. Bellotti, P.; Huang, H.-M.; Faber, T.; Glorius, F. Photocatalytic late-stage C–H functionalization. *Chem. Rev.* **2023**, *123*, 4237–4352. [CrossRef] [PubMed]
4. Zhou, L.; Martirez, J.M.P.; Finzel, J.; Zhang, C.; Swearer, D.F.; Tian, S.; Robatjazi, H.; Lou, M.; Dong, L.; Henderson, L.; et al. Light-driven methane dry reforming with single atomic site antenna-reactor plasmonic photocatalysts. *Nat. Energy* **2020**, *5*, 61–70. [CrossRef]
5. Li, C.; Kong, X.Y.; Lyu, M.; Tay, X.T.; Đokić, M.; Chin, K.F.; Yang, C.T.; Lee, E.K.X.; Zhang, J.; Tham, C.Y.; et al. Upcycling of non-biodegradable plastics by base metal photocatalysis. *Chem* **2023**, *9*, 2683–2700. [CrossRef]
6. Zhang, L.; Wu, Y.; Li, J.; Jin, Z.; Li, Y.; Tsubaki, N. Amorphous/crystalline heterojunction interface driving the spatial separation of charge carriers for efficient photocatalytic hydrogen evolution. *Mater. Today Phys.* **2022**, *27*, 100767. [CrossRef]
7. Pavliuk, M.V.; Wrede, S.; Liu, A.; Brnovic, A.; Wang, S.; Axelsson, M.; Tian, H. Preparation, characterization, evaluation and mechanistic study of organic polymer nano-photocatalysts for solar fuel production. *Chem. Soc. Rev.* **2022**, *51*, 6909–6935. [CrossRef]
8. Sun, P.; Xing, Z.; Li, Z.; Zhou, W. Recent advances in quantum dots photocatalysts. *Chem. Eng. J.* **2023**, *458*, 141399. [CrossRef]
9. Hao, J.; Liu, H.; Wang, K.; Sun, X.W.; Delville, J.-P.; Delville, M.-H. Hole scavenging and electron–hole pair photoproduction rate: Two mandatory key factors to control single-tip Au-CdSe/CdS nanoheterodimers. *ACS Nano* **2021**, *15*, 15328–15341. [CrossRef]
10. Chen, Q.; Liu, Y.; Mao, B.; Wu, Z.; Yan, W.; Zhang, D.; Li, Q.; Huang, H.; Kang, Z.; Shi, W. Carbon-dot-mediated highly efficient visible-driven photocatalytic hydrogen evolution coupled with organic osxidation. *Adv. Funct. Mater.* **2023**, 2305318. [CrossRef]
11. Kowalik, P.; Bujak, P.; Penkala, M.; Tomaszewski, W.; Lisowski, W.; Sobczak, J.W.; Siepietowska, D.; Maroń, A.M.; Polak, J.; Bartoszek, M.; et al. Ag-In-Zn-S quaternary nanocrystals prepared from $InCl_2$ precursor: Photophysical and spectroscopic properties and application as visible light photocatalysts of aromatic aldehyde photoreduction. *Chem. Mater.* **2023**, *35*, 6447–6462. [CrossRef]
12. Gong, G.; Liu, Y.; Mao, B.; Tan, L.; Yang, Y.; Shi, W. Ag doping of Zn-In-S quantum dots for photocatalytic hydrogen evolution: Simultaneous bandgap narrowing and carrier lifetime elongation. *Appl. Catal. B* **2017**, *216*, 11–19. [CrossRef]
13. Zhang, D.; Mao, B.; Li, D.; Liu, Y.; Li, F.; Dong, W.; Jiang, T.; Shi, W. 0D/2D Z-scheme heterojunctions of Zn-$AgIn_5S_8$ QDs/α-Fe_2O_3 nanosheets for efficient visible-light-driven hydrogen production. *Chem. Eng. J.* **2021**, *417*, 128275. [CrossRef]
14. Hu, J.; Shen, X.; Liu, A.; Lu, Z.; Xie, J.; Hao, A.; Jiang, X.; Wang, J.; Cao, Y. Highly dispersed Cu_2O quantum dots (about 2 nm) constructed by a simple functional group anchoring strategy boost the photocatalytic water splitting ability by 72 times. *J. Mater. Chem. A* **2023**, *11*, 1290–1300. [CrossRef]
15. Shen, H.; Wang, Y.-Z.; Liu, G.; Li, L.; Xia, R.; Luo, B.; Wang, J.; Suo, D.; Shi, W.; Yong, Y.-C. A whole-cell inorganic-biohybrid system integrated by reduced graphene oxide for boosting solar hydrogen production. *ACS Catal.* **2020**, *10*, 13290–13295. [CrossRef]
16. Xin, H.; Sun, L.; Zhao, Y.; Lv, Y.; Luo, Q.; Guo, S.; Li, D.; Mu, C.; Huang, B.; Ma, F. Size-controllable Rh_2P nanoparticles on reduced graphene oxide toward highly hydrogen production. *Chem. Eng. J.* **2023**, *466*, 143277. [CrossRef]
17. Yuan, C.; Lv, H.; Zhang, Y.; Fei, Q.; Xiao, D.; Yin, H.; Lu, Z.; Zhang, Y. Three-dimensional nanoporous heterojunction of CdS/np-rGO for highly efficient photocatalytic hydrogen evolution under visible light. *Carbon* **2023**, *206*, 237–245. [CrossRef]
18. Raja, A.; Son, N.; Swaminathan, M.; Kang, M. Effective graphene incorporation of strontium niobate–doped titanium oxide for photocatalytic hydrogen production. *J. Cleaner Prod.* **2023**, *423*, 138809. [CrossRef]
19. Samajdar, S.; Bera, S.; Das, P.S.; Finch, H.; Dhanak, V.R.; Chakraborty, S.; Maiyalagan, T.; Annapurna, K.; Ghosh, S. Exploration of 1D-2D $LaFeO_3$/RGO S-scheme heterojunction for photocatalytic water splitting. *Int. J. Hydrogen Energy* **2023**, *48*, 17838–17851. [CrossRef]
20. Chen, J.; Zhang, H.; Liu, P.; Li, Y.; Liu, X.; Li, G.; Wong, P.K.; An, T.; Zhao, H. Cross-linked $ZnIn_2S_4$/rGO composite photocatalyst for sunlight-driven photocatalytic degradation of 4-nitrophenol. *Appl. Catal. B* **2015**, *168–169*, 266–273. [CrossRef]
21. Lv, T.; Wu, M.; Guo, M.; Liu, Q.; Jia, L. Self-assembly photocatalytic reduction synthesis of graphene-encapusulated $LaNiO_3$ nanoreactor with high efficiency and stability for photocatalytic water splitting to hydrogen. *Chem. Eng. J.* **2019**, *356*, 580–591. [CrossRef]
22. Iwase, A.; Ng, Y.H.; Amal, R.; Kudo, A. Solar hydrogen evolution using a $CuGaS_2$ photocathode improved by incorporating reduced graphene oxide. *J. Mater. Chem. A* **2015**, *3*, 8566–8570. [CrossRef]
23. Xie, C.; Lu, X.; Deng, F.; Luo, X.; Gao, J.; Dionysiou, D.D. Unique surface structure of nano-sized $CuInS_2$ anchored on rGO thin film and its superior photocatalytic activity in real wastewater treatment. *Chem. Eng. J.* **2018**, *338*, 591–598. [CrossRef]
24. Yang, Y.; Mao, B.; Gong, G.; Li, D.; Liu, Y.; Cao, W.; Xing, L.; Zeng, J.; Shi, W.; Yuan, S. In-situ growth of Zn-$AgIn_5S_8$ quantum dots on g-C_3N_4 towards 0D/2D heterostructured photocatalysts with enhanced hydrogen production. *Int. J. Hydrogen Energy* **2019**, *44*, 15882–15891. [CrossRef]
25. Zhang, Y.; Qiu, J.; Zhu, B.; Fedin, M.V.; Cheng, B.; Yu, J.; Zhang, L. ZnO/COF S-scheme heterojunction for improved photocatalytic H_2O_2 production performance. *Chem. Eng. J.* **2022**, *444*, 136584. [CrossRef]
26. Koczoń, P.; Hołaj-Krzak, J.T.; Palani, B.K.; Bolewski, T.; Dąbrowski, J.; Bartyzel, B.J.; Gruczyńska-Sękowska, E. The analytical possibilities of FT-IR spectroscopy powered by vibrating molecules. *Int. J. Mol. Sci.* **2023**, *24*, 1013. [CrossRef]
27. Yang, L.; Guo, J.; Yu, Y.; An, Q.; Wang, L.; Li, S.; Huang, X.; Mu, S.; Qi, S. Hydrogen bonds of sodium alginate/Antarctic krill protein composite material. *Carbohydr. Polym.* **2016**, *142*, 275–281. [CrossRef]
28. Shen, L.; Li, Y.; Zhao, W.; Wang, K.; Ci, X.; Wu, Y.; Liu, G.; Liu, C.; Fang, Z. Tuning F-doped degree of rGO: Restraining corrosion-promotion activity of EP/rGO nanocomposite coating. *J. Mater. Sci. Technol.* **2020**, *44*, 121–132. [CrossRef]

29. Siddique, S.; Zain ul, A.; Waseem, M.; Naseem, T.; Bibi, A.; Hafeez, M.; Din, S.U.; Haq, S.; Qureshi, S. Photo-catalytic and anti-microbial activities of rGO/CuO nanocomposite. *J. Inorg. Organomet. Polym. Mater.* **2021**, *31*, 1359–1372. [CrossRef]
30. Durai, M.; Ahn, Y.-H. Photocatalytic H_2 generation under blue and white LEDs by Fe_2O_3 /KTLO/rGO S-scheme composite photocatalyst. *J. Alloys Compd.* **2023**, *965*, 171457. [CrossRef]
31. Hossen, M.A.; Khatun, F.; Ikreedeegh, R.R.; Muhammad, A.D.; Abd Aziz, A.; Leong, K.H.; Sim, L.C.; Lihua, W.; Monir, M.U. Enhanced photocatalytic CO_2 reduction to CH_4 using novel ternary photocatalyst RGO/Au-TNTAs. *Energies* **2023**, *16*, 5404. [CrossRef]
32. Zhao, X.; Gao, M.; Liu, Q.; Zhang, Y.; Wang, H.; Yang, G.; Huo, P. Reduced graphene oxide-modified Z-scheme g-C_3N_4/CdS photocatalyst with a staggered structure for the enhanced photoreduction of CO_2. *Sustain. Energy Fuels* **2022**, *6*, 3768–3777. [CrossRef]
33. Wang, T.; Yue, D.; Li, X.; Zhao, Y. Lead-free double perovskite $Cs_2AgBiBr_6$/RGO composite for efficient visible light photocatalytic H_2 evolution. *Appl. Catal. B* **2020**, *268*, 118399. [CrossRef]
34. Peng, X.; Ye, L.; Ding, Y.; Yi, L.; Zhang, C.; Wen, Z. Nanohybrid photocatalysts with $ZnIn_2S_4$ nanosheets encapsulated UiO-66 octahedral nanoparticles for visible-light-driven hydrogen generation. *Appl. Catal. B* **2020**, *260*, 118152. [CrossRef]
35. Du, C.; Yan, B.; Yang, G. Self-integrated effects of 2D $ZnIn_2S_4$ and amorphous Mo_2C nanoparticles composite for promoting solar hydrogen generation. *Nano Energy* **2020**, *76*, 105031. [CrossRef]
36. Jia, W.L.; Li, W.J.; Yuan, H.Y.; Wu, X.; Liu, Y.; Dai, S.; Cheng, Q.; Liu, P.F.; Yang, H.G. Surface Cu^+ modified $ZnIn_2S_4$ for promoted visible-light photocatalytic hydrogen evolution. *J. Energy Chem.* **2022**, *74*, 341–348. [CrossRef]
37. Zhang, L.; Jiang, D.; Irfan, R.M.; Tang, S.; Chen, X.; Du, P. Highly efficient and selective photocatalytic dehydrogenation of benzyl alcohol for simultaneous hydrogen and benzaldehyde production over Ni-decorated $Zn_{0.5}Cd_{0.5}S$ solid solution. *J. Energy Chem.* **2019**, *30*, 71–77. [CrossRef]
38. Guo, X.; Liu, X.; Yan, J.; Liu, S.F. Heterointerface engineering of ZnO/CdS heterostructures through ZnS Layers for photocatalytic water splitting. *Chemistry* **2022**, *28*, e202202662. [CrossRef]
39. Zhang, X.; Gao, M.; Qiu, L.; Sheng, J.; Yang, W.; Yu, Y. Sulfur vacancies-induced "Electron Bridge" in Ni_4Mo/S_v-$Zn_xCd_{1-x}S$ regulates electron transfer for efficient H_2-releasing photocatalysis. *J. Energy Chem.* **2023**, *79*, 64–71. [CrossRef]
40. Zhang, R.; Wan, W.; Li, D.; Dong, F.; Zhou, Y. Three-dimensional MoS_2/reduced graphene oxide aerogel as a macroscopic visible-light photocatalyst. *Chin. J. Catal.* **2017**, *38*, 313–320. [CrossRef]
41. Dhandapani, P.; AlSalhi, M.S.; Karthick, R.; Chen, F.; Devanesan, S.; Kim, W.; Rajasekar, A.; Ahmed, M.; Aljaafreh, M.J.; Muhammad, A. Biological mediated synthesis of RGO-ZnO composites with enhanced photocatalytic and antibacterial activity. *J. Hazard. Mater.* **2021**, *409*, 124661. [CrossRef] [PubMed]
42. Murillo Leo, I.; Soto, E.; Vaquero, F.; Mota, N.; Navarro, R.M.; Fierro, J.L.G. Influence of the reduction of graphene oxide (rGO) on the structure and photoactivity of CdS-rGO hybrid systems. *Int. J. Hydrogen Energy* **2017**, *42*, 13691–13703. [CrossRef]
43. Li, W.; Wang, F.; Chu, X.-S.; Liu, X.-Y.; Dang, Y.-Y. Regulation of bandgap and interfacial conductivity: Construction of carbon-doped three-dimensional porous h-BN/rGO hybrid for hydrogen evolution. *Appl. Surf. Sci.* **2021**, *560*, 150053. [CrossRef]
44. Chen, Y.; Mou, Z.; Yin, S.; Huang, H.; Yang, P.; Wang, X.; Du, Y. Graphene enhanced photocatalytic hydrogen evolution performance of dye-sensitized TiO_2 under visible light irradiation. *Mater. Lett.* **2013**, *107*, 31–34. [CrossRef]
45. Pan, B.; Wang, Y.; Liang, Y.; Luo, S.; Su, W.; Wang, X. Nanocomposite of $BiPO_4$ and reduced graphene oxide as an efficient photocatalyst for hydrogen evolution. *Int. J. Hydrogen Energy* **2014**, *39*, 13527–13533. [CrossRef]
46. Gupta, B.; Melvin, A.A.; Matthews, T.; Dhara, S.; Dash, S.; Tyagi, A.K. Facile gamma radiolytic methodology for TiO_2-rGO synthesis: Effect on photo-catalytic H_2 evolution. *Int. J. Hydrogen Energy* **2015**, *40*, 5815–5823. [CrossRef]
47. Li, D.; Zhao, H.; Li, L.; Mao, B.; Chen, M.; Shen, H.; Shi, W.; Jiang, D.; Lei, Y. Graphene-Sensitized Perovskite Oxide Monolayer Nanosheets for Efficient Photocatalytic Reaction. *Adv. Funct. Mater.* **2018**, *28*, 1806284. [CrossRef]
48. Li, F.; Liu, Y.; Chen, Q.; Gu, X.; Dong, W.; Zhang, D.; Huang, H.; Mao, B.; Kang, Z.; Shi, W. Transient photovoltage study of the kinetics and synergy of electron/hole co-extraction in MoS_2/Ag-In-Zn-S/carbon dot photocatalysts for promoted hydrogen production. *Chem. Eng. J.* **2022**, *439*, 135759. [CrossRef]